

## Overview on ASDEX Upgrade Results

O. Gruber, R. Arslanbekov, C. Atanasiu<sup>1</sup>, A. Bard, G. Becker, W. Becker, M. Beckmann, K. Behler, K. Behringer, A. Bergmann, R. Bilato, D. Bolshukin, K. Borrass, H.-S. Bosch, B. Braams<sup>2</sup>, M. Brambilla, R. Brandenburg<sup>3</sup>, F. Braun, H. Brinkschulte, R. Brückner, B. Brüsehaber, K. Büchl, H. Bürbaumer<sup>3</sup>, A. Buhler, A. Carlson, M. Ciric, G. Conway, D. Coster, C. Dorn, R. Drube, R. Dux, S. Egorov<sup>4</sup>, W. Engelhardt, H.-U. Fahrbach, U. Fantz<sup>5</sup>, H. Faugel, M. Foley<sup>6</sup>, P. Franzen, P. Fu<sup>7</sup>, J. C. Fuchs, J. Gafert, G. Gantenbein<sup>8</sup>, O. Gehre, A. Geier, J. Gernhardt, E. Gubanka, A. Gude, S. Günter, G. Haas, D. Hartmann, B. Heinemann, A. Herrmann, J. Hobirk, F. Hofmeister, H. Hohenöcker, L. Horton, L. Hu<sup>7</sup>, D. Jacobi, M. Jakobi, F. Jenko, A. Kallenbach, O. Kardaun, M. Kaufmann, A. Kendl, J.-W. Kim, K. Kirov, R. Kochergov, H. Kollotzek, W. Kraus, K. Krieger, B. Kurzan, G. Kyriakakis<sup>9</sup>, K. Lackner, P. T. Lang, R. S. Lang, M. Laux, L. Lengyel, F. Leuterer, A. Lorenz, H. Maier, K. Mank, M.-E. Manso<sup>10</sup>, M. Maraschek, K.-F. Mast, P. McCarthy<sup>6</sup>, D. Meisel, H. Meister, F. Meo, V. Mertens, R. Merkel, J. P. Meskat<sup>8</sup>, R. Monk, H. W. Müller, M. München, H. Murmann, G. Neu, R. Neu, J. Neuhauser, J.-M. Noterdaeme, I. Nunes<sup>10</sup>, G. Pautasso, A. G. Peeters, G. Pereverzev, S. Pinches, R. Pugno, G. Raupp, T. Ribeiro<sup>10</sup>, R. Riedl, S. Riondato, V. Rohde, H. Röhr, J. Roth, F. Ryter, H. Salzmann, W. Sandmann, S. Sarelma, S. Schade, H.-B. Schilling, D. Schlögl, K. Schmidtman, R. Schneider, W. Schneider, G. Schramm, J. Schweinzer, S. Schweizer, B.D. Scott, U. Seidel, F. Serra<sup>10</sup>, S. Sesnic, C. Sihler, A. Silva<sup>10</sup>, A. Sips, E. Speth, A. Stäbler, K.-H. Steuer, J. Stober, B. Streibl, E. Strumberger, W. Suttrop, A. Tabasso, A. Tanga, G. Tardini, C. Tichmann, W. Treutterer, M. Troppmann, N. Tsois<sup>9</sup>, W. Ullrich, M. Ulrich, P. Varela<sup>10</sup>, O. Vollmer, U. Wenzel, F. Wesner, R. Wolf, E. Wolfrum, R. Wunderlich, N. Xantopoulos<sup>9</sup>, Q. Yu<sup>7</sup>, M. Zarrabian, D. Zasche, T. Zehetbauer, H.-P. Zehrfeld, A. Zeiler, H. Zohm

Max-Planck-Institut für Plasmaphysik, EURATOM-IPP Assoc., 85748 Garching, Germany

<sup>1</sup> Inst. Atomic Physics, Bucharest, Romania

<sup>2</sup> New York University, NJ, USA

<sup>3</sup> Technical University of Vienna, Austria

<sup>4</sup> Efremov Institute, St. Petersburg, CIS

<sup>5</sup> University of Augsburg, Germany

<sup>6</sup> University College Cork, Republic of Ireland

<sup>7</sup> Academia Sinica, Hefei, China

<sup>8</sup> IPF, University of Stuttgart, Germany

<sup>9</sup> NSCR Demokritos, Athens, Greece

<sup>10</sup> Centro de Fusão Nuclear, Lisbon, Portugal

e-mail contact of main author: gruber@ipp.mpg.de

**Abstract.** Ion and electron temperatures in conventional H mode on ASDEX Upgrade are stiff and limited by a critical temperature gradient length  $\nabla T/T$  as given by ion temperature gradient (ITG) driven turbulence. ECRH experiments indicate that  $T_e$  profiles are also stiff as predicted by ETG turbulence with streamers. Accordingly, core and edge temperatures are proportional to each other and plasma energy is proportional to pedestal pressure for fixed density profiles. Density profiles are not stiff, and confinement improves with density peaking. Higher triangular shapes ( $\delta < 0.45$ ) show strongly improved confinement up to Greenwald density  $n_{GW}$  due to increasing pedestal pressure, and H-mode density operation extends above  $n_{GW}$ . Density peaking at  $n_{GW}$  was achieved with controlled gas puff rates and first results from higher high field side pellet velocities are promising. At  $n_{GW}$  small type II ELMs provide good confinement with low divertor power loading. In advanced scenarios highest performance was achieved in improved H-modes with  $H_{L-89P}\beta_N \approx 7.2$  at  $\delta = 0.3$ , limited by neo-classical tearing modes (NTM) at low central shear ( $q_{min} \approx 1$ ). The T profiles are still governed by ITG/TEM turbulence and confinement is improved by density peaking. Ion internal transport barriers (ITB) discharges with reversed shear and L-mode edge are limited to  $\beta_N \leq 1.7$  by ideal MHD modes and got  $H_{L-89P} \leq 2.1$ . Turbulent transport is suppressed in agreement with ExB shear flow paradigm, and transport coefficients are at neo-classical ion transport level. Reactor-relevant ion and electron ITBs with  $T_e \approx T_i \approx 10$  keV were achieved by combining ion and electron heating (NI, ECRH). Full non-inductive current drive was achieved in integrated high performance H-mode scenario with  $\bar{n}_e = n_{GW}$ ,  $\beta_p = 3.1$  and  $H_{L-89P} = 1.8$ , which developed ITBs with  $q_{min} \approx 1$ . Central co-ECCD at low densities allowed high current drive fraction of  $> 80\%$ , while counter-ECCD leads to negative central shear and electron ITB with  $T_e(0) > 10$  keV. MHD phenomena, especially fishbones, contribute to achieve quasi-stationary advanced discharge conditions and trigger ITBs, but also limit the operation of conventional and advanced scenarios. Complete NTM stabilisation has been demonstrated using ECCD with 10% of heating power. Extension of MHD limits is expected from using off-axis CD (tangential NI) and wall stabilisation. Presently, divertor shape is adapted to higher  $\delta$ 's and tungsten covering of first wall is extended based on the positive experience using tungsten on divertor and heat shield tiles.

## 1. Introduction

The ASDEX Upgrade non-circular tokamak programme has been largely focused on (i) performance-related physics in the ITER base-line scenario, the ELMY H-mode near operational limits, (ii) investigation of scenarios and physics of advanced tokamak plasma concepts with internal transport barriers leading to enhanced performance and possibly stationary operation, (iii) MHD stability and active stabilisation of beta limiting instabilities, and (iv) edge and divertor physics in these high-confinement regimes, with the aim of optimising power exhaust and particle control (ash removal).

The similarity of ASDEX Upgrade to ITER in poloidal field coil system and divertor configuration makes it particularly suited to testing control strategies for plasma performance. Neutral beam injection (NI) was available with injection energies up to 100 keV (20 MW), which allowed studies of influence of heat deposition on transport and of fast particle effects. Minority heating with ICRH (up to 5.7 MW coupled) was used for central heating at high densities, and to study influence of deep particle refuelling and toroidal rotation by substituting NI. ECRH system (coupled power of 1.4 MW) allowed pure electron heating, transport studies and feedback stabilisation of NTMs. Provisions for current drive and active control of current profile in advanced scenarios were available with nearly perpendicular NI and ECRF using steerable mirrors (up to 350 kA driven on-axis). Experiments using on-axis fast wave or off-axis mode conversion CD with ICRF have been started.

The present version of the closed divertor (vertical target plates including a roof baffle, cryopump), which is rather similar to the ITER-FEAT reference design, allows a strong reduction of heat flux to target plates and is capable of handling heating powers of up to 20 MW. The observed strongly reduced, distributed power flux to surrounding structures during both ELM and ELM-free phases is in agreement with B2-Eirene simulations [1]. The studies of reactor-compatible materials was continued by covering parts of the low field side (LFS) heat shield with tungsten [2].

High shaping capability with elongations  $\kappa \leq 1.8$  and triangularities  $\delta$  up to 0.45 at the separatrix allowed to study the influence of plasma shape on performance and operational limits. Such equilibria have been run with the outer strike point being on the top of the roof baffle or on the outer vertical target to get higher pumping speeds. Additionally, the similarity in cross-section to other divertor tokamaks is important in determining size scalings for core, edge and divertor physics. This collaborative work, including extrapolation to ITER parameters, has continued and was even enhanced in the new JET operation under EFDA. For the promising refuelling by pellet injection first results were obtained from a new high field side (HFS) pellet launcher, capable of injection speeds of up to 1000 m/s.

The following sections report on recent progress made in ASDEX Upgrade experiments since the last IAEA conference [3], viz. ion and electron temperature profile stiffness (Sect. 2, [4,5]), high density H-mode operation, namely confinement, density profile peaking, HFS pellet injection and tolerable Type-II ELMs (Sect.3, [4,5,6]). Cold pulse and impurity transport studies are not reported on here [7,8]. The next sections are devoted to advanced scenarios as improved H-mode, ion ITBs and reactor relevant combined ion and electron ITBs (Sect. 4, [4,5,9,10]), fully non-inductively driven discharges at high  $\beta_p$  and with ECCD exhibiting electron ITBs (Sect. 5, [9,10]). stabilisation of neo-classical tearing modes by ECCD (Sect. 6, [11,12]), MHD in advanced scenarios (Sect. 7, [10]), and finally operation with high-Z wall coatings (Sect. 8, [2]).

## 2. Temperature profile stiffness

As reported earlier [3,13,14], ion temperature ( $T_i$ ) profiles in conventional H-mode discharges of ASDEX Upgrade are generally "stiff": temperature profiles are limited by a maximum value of  $\nabla T/T$ , the inverse temperature gradient length  $L_T$ . At medium and high densities the electron temperatures ( $T_e$ ) show the same behaviour, as they are closely coupled to  $T_i$  and heated as well by NI. Turbulence driven by Ion Temperature Gradient (ITG) is believed to be the main origin of turbulence causing the anomalous transport through the ion channel [15,16]. It leads to limitation of  $T_i$  at a critical value of  $\nabla T/T$  as observed. The transport properties of temperature gradient (TG) driven turbulence can be expressed for the heat diffusivity by two additive terms. One term represents transport without TG turbulence, for instance neo-classical transport for ions, while the other represents the transport by TG turbulence. This term is equal

to zero for  $\nabla T/T < (\nabla T/T)_c$ , but increases strongly when  $\nabla T/T > (\nabla T/T)_c$  and may saturate. Then transport is high and keeps the profiles close to  $(\nabla T/T)_c$ . Gyro-Bohm scaling  $\chi_{gB} \propto T^{3/2}$  of this term causes an increase of stiffness with temperature. These considerations are not necessarily valid inside the sawtooth inversion radius where profiles may be limited by the MHD activity or at edge where the temperatures may be too low. The profile stiffness reflects a strong coupling between core and H-mode pedestal temperatures or, equivalently, profiles plotted on logarithmic scale are shifted vertically according to their edge temperature (Fig. 1).

## 2.1 Temperature profile stiffness in NI-heated H-modes

This profile stiffness was confirmed by comparing the influence of rather different heat deposition profiles using 60 keV and 93 keV NI beams at high plasma densities ( $\bar{n}_e \approx 10^{20} \text{ m}^{-3}$ ): measured  $T$  profiles are unaffected. The reaction of the transport coefficients to these different heating power profiles is as expected. For the deeper deposition the  $\chi_{\text{eff}}$  increases by almost a factor of two compared to the more off-axis deposited power. Obviously, the heat conductivity adjusts itself to maintain the observed stiff temperature profiles, and is not anymore a usable description of transport behaviour.

In addition to these studies, a database including profile data from about 30 H-mode discharges with NI [5,16] indicates that  $T_i$  and  $T_e$  profiles are quite stiff at medium and high densities. Simulations of these discharges using three models based on ITG and including trapped electron mode physics and ExB shear flow, IFS/PPPL [15], GLF23 [17], Weiland [18], agree well with these data and confirm the ITG turbulence as the driving mechanism. In the simulations the boundary condition for the temperature (applied at  $r/a=0.8$ ) as well as the density profiles are taken from the experiment.

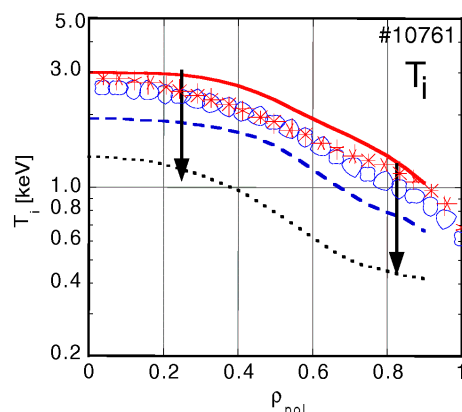


Fig. 1 H-mode ion temperature profiles are stiff during a density ramp up (lines) and remain fixed for on- and off-axis heat deposition (symbols, same heating power) with temperature gradient length  $T/\nabla T \approx R/5$ .

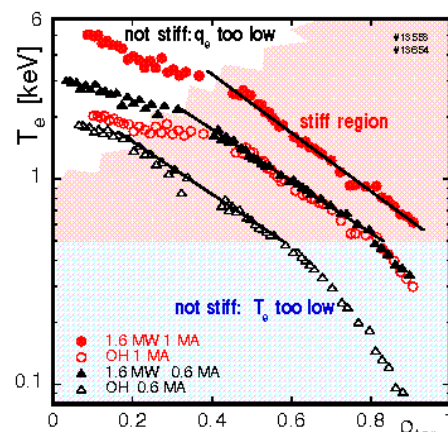


Fig. 2 Stiff  $T_e$  profiles for pure ohmic heating and additional central ECRH (1.6 MW) at two plasma currents.

## 2.2 Electron temperature profile stiffness with strong electron heating

Recent calculations [19] indicate that Electron Temperature Gradient (ETG) turbulence is able to drive a large electron heat transport because large cells, so-called streamers, can develop. The properties of temperature gradient driven turbulence for ions and electrons are qualitatively similar as has been confirmed on ASDEX Upgrade discharges with  $T_e > T_i$  using ECRH in steady-state and power modulation experiments [4].

Central heating with ECRH at different plasma currents resulted in similar shapes of the electron temperature profiles, which are shifted according to their edge temperatures in the logarithmic scale of Fig. 2. The shadowed area indicates a region where the slope of the profiles, i.e.  $\nabla T/T$ , is the same. In the centre the slope is different for each profile. Obviously the heat flux to the electron channel is not high enough to reach  $(\nabla T/T)_c$ . Towards the edge the profiles gradually deviate from the constant slope at  $T_e < 600 \text{ eV}$ . In the stiff region the value of  $\nabla T/T$  does not depend on  $I_p$  which implies that confinement improvement with  $I_p$  is provided by higher edge temperatures.

Electron heat diffusivities from power balance analyses exhibit the expected properties, namely small  $\chi/T^{3/2}$  values for  $\nabla T_e/T_e < 8 \text{ m}^{-1}$  and a strong increase above this threshold [4]. The

stiffness increases with higher temperatures in qualitative agreement with ETG calculations indicating that the appearance of streamers requires a critical temperature [19].

These steady-state analyses were extended with ECRH modulation experiments confirming the electron temperature stiffness. These investigations revealed further that changes in transport for off-axis ECH cases are caused by a change of diffusivity and cannot be attributed to convection [4]. In the stiff region, the heat pulses propagating outwards and inwards yield different values for the derived  $\chi^{HP}$  by the fact that heat pulses tend to locally increase or decrease  $\nabla T/T$  depending on their direction of propagation. The  $\chi^{HP}$  values are above the  $\chi$ 's derived from power balance and their ratio strongly increases with temperature characterising the profile stiffness. Accordingly, differences in heat pulse propagation between deuterium and hydrogen discharges at same discharge parameters, but at different resulting temperatures, can be reconciled by the T dependence of the stiffness.

### 3. High density H-mode operation

#### 3.1 Influence of non-stiff density profiles and triangularity on energy confinement

To achieve high fusion yield by high central density and low power load in the divertor with sufficient SOL density a fusion reactor has to operate at densities close to  $n_{GW}$ . But confinement degrades at high line averaged densities  $\bar{n}_e$ , while it is improving with  $\bar{n}_e$  at low densities. This is a consequence of temperature profile stiffness ( $T_{core} \propto T_{ped}$ ), the nearly fixed pedestal pressure of the edge H-mode barrier limited by MHD stability, and the fact, that density profiles tend to be not stiff. At low densities more peaked density profiles are observed, while increasing the density by gas puffing leads to density profile broadening and the edge density increases strongly compared with the line averaged density [3]. Correspondingly the stored energy is even decreasing with increasing  $\bar{n}_e$  and stiff T profiles in contrast to the ITER confinement time scalings.

For a given shape of the density profile, the plasma energy is expected to be proportional to the pedestal pressure. This is indeed confirmed for  $\bar{n}_e < 0.8 n_{GW}$  where a strong correlation between electron pedestal pressure (at  $\rho=0.8$ ) and thermal plasma energy is seen

$$W_{th} \propto p_{e,ped}^{0.75} P_h^{0.14} \quad \text{with low RMSE value of about 10\% [4].}$$

This representation provides a unification of discharges with different ELM types,  $I_p$ 's and triangularities ( $0.1 < \delta < 0.4$ ), which only act on confinement via the edge pressure, namely as:

$$p_{e,ped} \propto I_p^{1.4} P_h^{0.2} \delta^{0.3}.$$

The dependence upon  $I_p$  does not quite reach  $I_p^2$  expected from MHD stability, which might be due to changes of other quantities in the edge region influencing stability, e.g. magnetic shear.

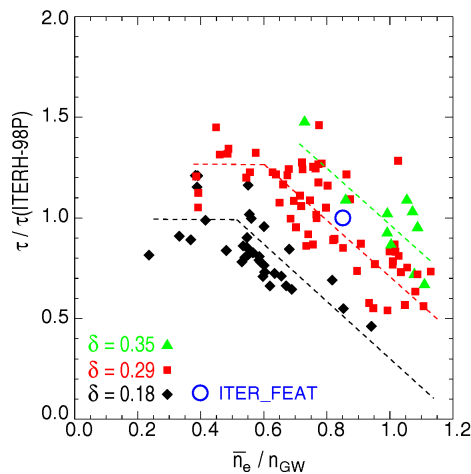


Fig. 3 Normalised thermal energy confinement vs. normalised line averaged density at different triangularities  $\delta$

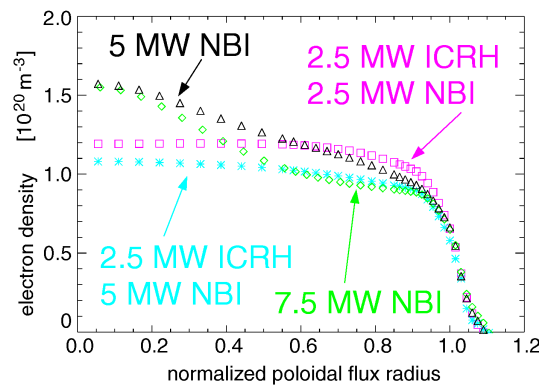


Fig. 4 Comparison of electron density profile peaking in H-mode at Greenwald density with moderate gas puffing using different heating scenarios.

An overview of the confinement data is provided in Fig.3 for  $\tau_E$  normalised by IPB98(y) ELMy H-mode scaling, the  $H_{H-98P}$ -factor. The positive density dependence in IPB98(y) which accentuates the confinement degradation at high densities by an even stronger decrease of the H-factor. The benefits resulting from higher triangular plasma shapes are demonstrated first in

enhanced confinement with  $H_{H-98P} \approx 1$  at  $n_{GW}$  due to higher pedestal pressures. Then back-transition into the L-mode at high densities is shifted to densities above  $n_{GW}$  extending the operation regime of the H-mode substantially. But it also exhibits a large scatter at given value of  $\bar{n}_e/n_{GW}$ . This scatter can be attributed to the non-stiff density profiles, which, besides being more peaked at low density than at higher ones, can vary depending on discharge scenario. This is taken into account in a regression by including the central density  $n_e(0)$  and the density in the scrape-off layer,  $n_{e,SOL}$ , yielding the following expression:

$$\tau_{E,th} \propto I_p^{1.0} P_h^{-0.56} \delta^{0.2} n_e(0)^{0.3} n_{e,SOL}^{-0.17} \quad (\text{RMSE: 9\%}) \quad [4].$$

This expression reflects the good confinement for peaked density profiles and confinement degradation with gas puffing represented by  $n_{e,SOL}$ . It is also in agreement with the  $W_{th}$  and  $p_{e,ped}$  scalings given before. The low RMSE is provided by the fact that this variable set takes account for the physics background.

### 3.2 Density profile peaking with constant gas puffing and HFS pellet injection

Density ramps using strong gas puffing causes high edge densities with its negative effect on global confinement. With "soft" density control or low external gas flux  $\bar{n}_e$  increases slowly on a time scale of a second (many energy confinement times) and can exceed Greenwald density [4]. After an initial decrease the confinement time itself it increases again and  $H_{H98-P} \approx 1$  is restored. The density profile shape broadens first because of increasing edge density, but on the longer time scale the density profiles peaks significantly, as shown in Fig. 4 for 5 MW NI. In this phase the edge region remains unchanged, as well as the stiff temperature profiles. As explained above, the non-stiff density profiles together with stiff T profiles are the reason for the confinement changes. Finally, good confinement is lost due to high central radiation caused by the loss of sawteeth leading to impurity accumulation in centre. Before accumulation  $Z_{eff}$  is below 1.3 in the core.

The operational window for the density profile peaking seems to be limited by a correlation between heat and particle transport. The heat flux was changed by increasing the heating power or its deposition profile combining NI (slightly hollow heating profile) and ICRF minority heating (central deposition). Thereby the region with density peaking is shrinking with increasing heating power and density profiles become even flat when central heating is increased (Fig. 4). In the latter case the particle source by NI is not changed, and cannot be the reason for the loss of density peaking therefore. The increase of central power deposition in both cases with its increase in transport at limited  $\nabla T/T$  is responsible for the density flattening. In summary, an inward particle pinch is involved (Ware pinch may be sufficient) which is cancelled by increasing outward diffusion at higher central heating.

These observations are supported by applying ECRH in various types of discharges which react to this additional heating with flatter density profiles. One may speculate that ECRH increases the electron heat flux and thus the ETG turbulence level. This so-called density "pump-out" was observed earlier in other devices too.

Injection of frozen hydrogen pellets from the magnetic LFS showed in strongly heated plasmas poor fuelling efficiency. In contrast, pellet injection from HFS first performed on ASDEX Upgrade was found to give significant higher efficiency, resulting in H-mode discharges well above the Greenwald density with high confinement properties [20]. This is due to the fast radial drift in the toroidal field gradient of the high- $\beta$ -plasmoid which is formed around the ablating pellet which transfers the pellet particles towards the plasma centre [21]. In both injection scenarios prompt convective particle and energy losses resulting from pellet induced ELM bursts within 10-20 ms after injection limit performance.

To overcome this problem the pellet must be deposited beyond the ELMing region at the edge by higher launch velocities. The new HFS pellet launcher will allow pellet velocities up to 100 m/s [6,22]. At velocity of 560 m/s a deeper pellet penetration and particle deposition towards the centre was found, mitigating the fast convective losses connected with the "pellet ELMs" (Fig. 5). But also the pellet induced ELMs are alleviated. Further optimisation of the looping system should enable us to define the demands of pellet injection systems for future large scale devices.

### 3.3 Tolerable Type-II ELMs close to the Greenwald density

H-modes with type I ELMs exhibit the best confinement performance, but the connected large power load during the ELM activity may not be acceptable in a reactor. Type III ELMs show

nearly no additional heat load on targets, but they are connected with confinement degradation. On ASDEX Upgrade small high frequency type-II ELMs were identified for  $q_{95} > 4.2$  and  $\delta > 0.4$  close to a double null configuration, but in contrast to earlier experiments [23] at the Greenwald limit [4]. This new result is quite attractive for a future reactor. The confinement is almost as good as with type-I ELMs and significantly higher than for type-III ELMs, providing  $\tau_E/\tau_{H98-P} \approx 0.95$ . The thermography data of the divertor target plates show that the peak power load is strongly reduced with type-II ELMs, reaching at most  $2 \text{ MW/m}^2$  almost without peaks on the outer plate, in comparison to  $5 \text{ MW/m}^2$  for type-I ELMs (Fig. 6). The power flux on the inner plates is always very low under these conditions. Magnetic measurements indicate that type-II ELMs often have a precursor at 15 to 30 kHz, indicating that they are MHD events indeed. Their signatures are different from those of type-III ELMs and they provide better confinement because they preserve the high edge pressure.

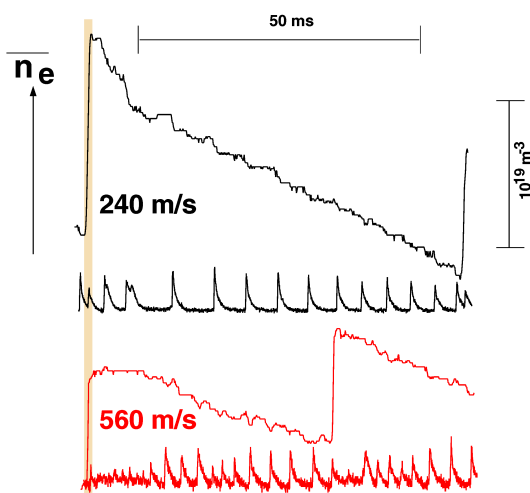


Fig. 5 Density decay after HFS pellet injection at two velocities and ELM activity ( $D\alpha$  in divertor). The initial density decay time increases from 48 ms ( $v=240 \text{ m/s}$ ) to 58 ms at higher velocity (average from several traces). The pellet induced ELM activity is reduced at the higher pellet speed.

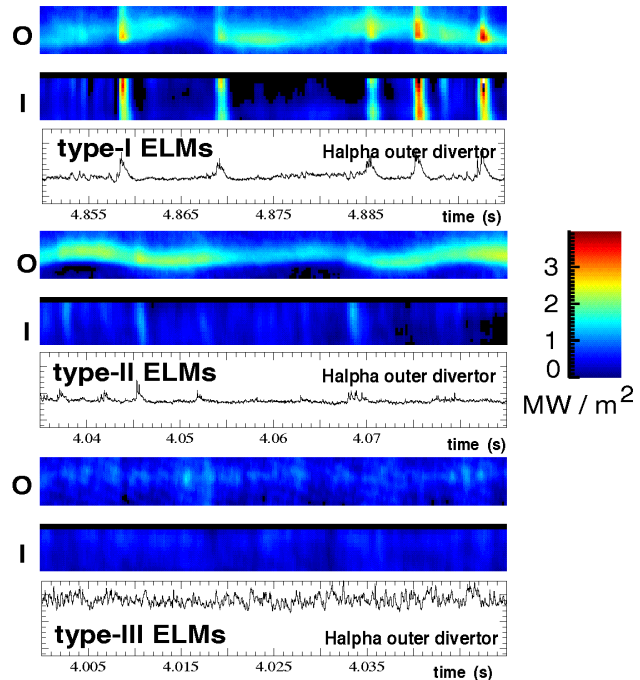


Fig. 6 Heat fluxes to the outer (o) and inner (i) strike point regions from infrared thermography for type I, II and III ELMs. The height of each bar corresponds to a poloidal length of 7 cm along the target surface.

#### 4. Advanced tokamak discharges

Advanced tokamak scenarios aim at an operating regime with improved confinement and stability properties (high normalized  $\beta_N = \beta / (I_p / (aB_t)) > 3$ ), thus allowing a reduced size tokamak reactor at lower  $I_p$  to be operated in steady state [24,25]. Internal transport barriers (ITBs), characterised by large pressure gradients in the region of reduced plasma turbulence, intrinsically drive bootstrap currents, which can constitute a significant part of the plasma current. For steady state operation the inductive driven plasma current has to be completely replaced by external non-inductively driven currents (in addition to the bootstrap current). Two advanced scenarios have been investigated by modifying the current density profile by means of early heating in the current ramp. All are connected with peaked profiles of density and toroidal rotation velocity. One is with improved core confinement in combination with H-mode edge barrier and a flat central  $q$ -profile, offering stationary, inductively driven improved H-mode operation [25,26,27]. This scenario may allow ignition even in the ITER-FEAT device. Secondly, ITBs with mainly reversed magnetic shear (RS) and  $q_{\min} > 1.5$  exhibit, at least in combination with an L-mode edge, bootstrap currents above 50% of the plasma current [25,27,28,29]. A combination of ITBs and H-mode edge is needed for steady-state, non-inductively driven tokamak operation combining improved performance and high bootstrap current fraction.

## 4.1 Improved H-mode

This regime is obtained with low pre-heating in the current ramp up and power increase afterwards causing a transition into the H-mode. A stationary state is obtained for up to 40 energy confinement times and several internal current diffusion times and is only limited by available pulse length [3,25,26]. Continuously reconnecting (1,1) fishbones clamp the current profile and lead to stationary central zero shear with  $q_{\min} \approx 1$  (see Sect. 7.1) [26,27,28].

The density was extended up to slightly below half of  $n_{GW}$  to integrate appropriate divertor conditions. With gas fuelling, the threshold heating power for ITB formation had to be raised by  $\approx 50\%$ . A density increase caused by improved core particle confinement at more triangular plasma shapes does not change the ITB onset conditions and allows higher  $\beta_N$ -values up to 2.6 without destabilising NTMs. The confinement increases to  $H_{H98-P}=1.7$  or  $H_{L89-P}=3$ , which is to the larger part given by the increasing pedestal pressure with higher  $\delta$  [25,27]. The more effective impurity screening at higher edge densities reduces  $Z_{\text{eff}}$  from 3 (at  $0.35 n_{GW}$ ) to 2 in the plasma centre. No temporal accumulation of impurities is observed, but impurities show centrally peaked densities consistent with neo-classical predictions.

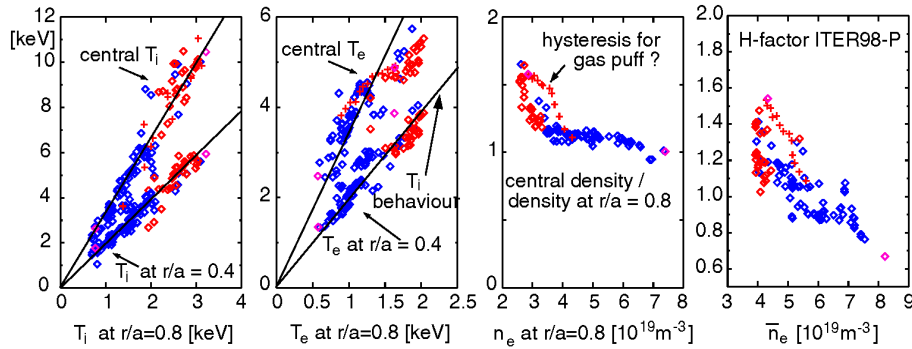


Fig.7 Comparison of temperature and density profiles and  $H_{H-98P}$  factor of standard and improved H-mode (density scan  $0.3 < \bar{n}_e/n_{GW} < 0.6$  at  $I_p=1$  MA,  $P_{NI}=5$  MW,  $\delta=0.2$ ).

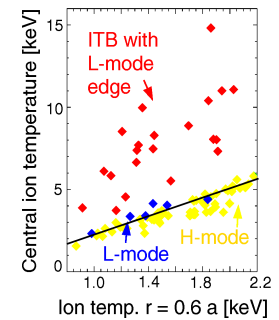


Fig. 8 Comparison of temperature profile peaking for different confinement modes.

Detailed studies have shown that the confinement physics in this regime can be largely unified with that of the standard H-mode. In the density scan of Fig. 7 improved H-mode shots have in general a lower  $\bar{n}_e$  and higher central as well as edge ion temperature. In all discharges the ion temperature profile is stiff by the fact that core (at  $r=0$  and  $r/a=0.4$ ) and edge ( $r/a=0.8$ ) temperatures are proportional to each other. The electron temperatures deviate from the linear dependence at lower density (higher  $T_e$ 's) where electron heating is reduced. The density profiles peak strongly at  $\bar{n}_e$  below  $4.5 \cdot 10^{19} \text{ m}^{-3}$ , correlated with the flattening of the central electron temperature. These data sets allow the following conclusions. First, the high ion core temperatures of improved H-mode can be explained by T stiffness alone. The roughly constant pressure at the pedestal top at fixed  $\delta$  allows for higher ion edge temperatures at lower edge densities, and due to T stiffness also the core temperatures increase. But  $\nabla T_i$  is still limited by profile stiffness. The density peaking in the improved H-mode leads to an increase of the plasma energy of up to 35%. The H-factor increases even up to 1.6, due to the density dependence in the scaling law  $\tau_{H-98P} \propto \bar{n}_e^{0.41}$ . In conclusion, the improved H-mode can be defined through the peaked density profiles. Moreover, the confinement scaling given in sect. 3.1 describes the good confinement of improved H-mode as well. Both  $T_i$  and  $T_e$  profiles in the region  $0.4 < r/a < 0.8$  can successfully be modelled with the ITG/TEM models confirming the above conclusions.

Density peaking may be due to the zero magnetic shear in the centre. Substitution of NI by ICRF minority heating leads to gradual suppression of fishbone activity and reappearance of sawteeth. As long as sawtooth periods are very long compared with energy confinement time the central  $q$ -profile remains flat and density peaking together with plasma energy is kept high. Increasing ICRF power finally leads to higher sawtooth activity connected with disappearance of strong density peaking and high H-factor. ITG stabilisation by  $E_r \times B$  shear flows seems not to be as important, as toroidal plasma rotation, the main driver for the  $E_r$  field (see also Sect. 4.2), is already decreasing with addition of 25% ICRH power.

## 4.2 Ion ITBs with strong ion heating

On ASDEX Upgrade ITBs for ions, for electrons (Sect. 5.2) and reactor relevant ion and electron ITBs with  $T_e \approx T_i \approx 10$  keV are obtained. Most of the ion ITBs are obtained through significant heating up to 7.5 MW in the current ramp up, producing RS with  $q_{\min} > 2$ . Without external current drive, however, the central RS cannot be sustained for more than about 1s. The ITBs are characterised by an ion  $\nabla T$  length being much smaller than that of H or L-mode plasmas determined by ITG turbulence and central  $T_i$  in excess of 10keV (see Fig. 8, 9) [5,9]. H-mode was prevented through limiter contact or upper single null (SN) configurations with unfavourable ion  $\nabla B$  drift allowing higher power levels [9]. At higher powers an expanding ITB region associated with an outward shift of the  $q_{\min}$  radius is obtained ( $H_{H-98P}$  reaches 1.2). The  $q_{\min}$  radius is always well aligned with the foot of the transport barrier (Fig. 9). The often disruptive termination of these discharges is caused by coupling of low (m,n) ideal internal modes (driven by large pressure gradients) to external kinks (see Sect. 7). This tendency is increased with H-mode transition, as the associated edge bootstrap current favours external kinks. The theoretical stability limit without a conducting wall has been calculated using the GATO code [10] yielding a critical  $\beta_N = 1.7$  in agreement with the experimental limit. With strong internal ion transport barriers the turbulence in the core is suppressed, as is confirmed by reflectometry signals. The  $E_r \times B$  shearing rate largely exceeds the linear ITG growth rates obtained from the GLF23 model [17] in the centre

$$\omega_{E \times B} = \left| (RB_p/B_t) \partial(E_r/RB_p)/\partial r \right| > \gamma_{\max, \text{ITG}},$$

and is of the same order as the growth rate at the foot of the barrier ( $r/a=0.6$ , Fig. 11) [5]. The

radial electric field  $E_r = \nabla_r p / (en_e) - v_t B_p + v_p B_t$  ( $v_p$ ,  $v_t$  poloidal, toroidal rotation velocities) is mainly determined by the toroidal velocity, as the contributions of the poloidal rotation and the pressure gradient at the ITB itself are smaller. Thereby, shearing rates from the measured poloidal rotation are in general larger than predicted by neo-classical theory, but the error bars on these measurements are rather large too. We have found that the Shafranov shift plays an important role in bringing down the linear growth rates to levels where they are below the ExB shearing rate [5]. The central Shafranov shift is large because both pressure and safety factor with RS are large on axis.

For suppressed turbulence and strong ion ITBs the ion heat transport is expected to be reduced to the neo-classical level. In fact the analysed ion heat diffusivities are even below standard neo-classical theory (Fig. 9). Standard neo-classical theory breaks down close to the axis because the radial size of the orbits is no longer small compared with the minor radius of the flux surface especially in RS discharges. As recent theories [30,31] got strong contradicting results Monte Carlo simulations have been performed [5]. Experimental and simulated heat conductivity reasonably agree (Fig. 9).

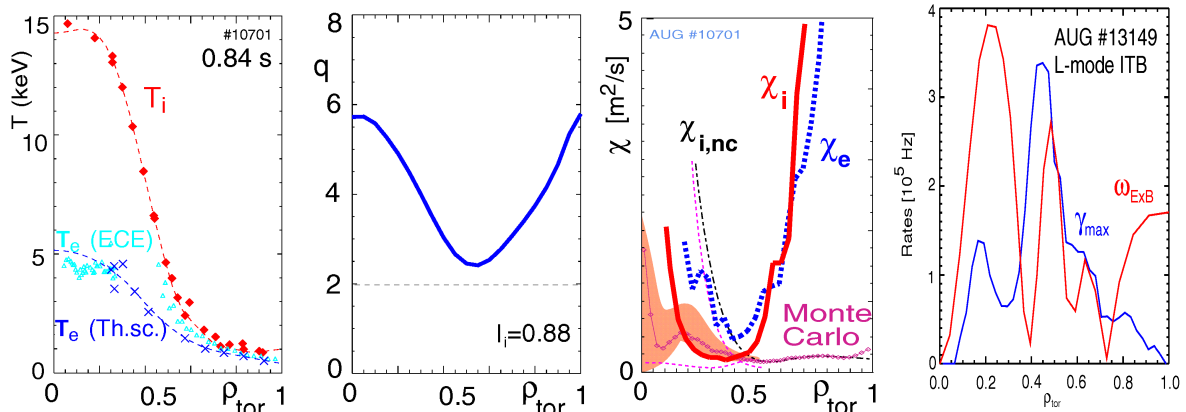


Fig.9 Ion ITB L-mode discharges: Temperature,  $q$  and heat diffusivity profiles.

*Ion neo-classical transport is calculated from Monte-Carlo simulations (1 MA, 2.5 T, 5 MW NI).*

*Standard neo-classical and potato orbit corrected [30,31] predictions are given by dotted curves.*

*$\omega_{E \times B}$  shearing rate and linear ITG growth rate  $\gamma_{\max}$  (1 MA, 2.5 T, 7.5 MW NI)*

### 4.3 Reactor relevant combined ion and electron ITBs

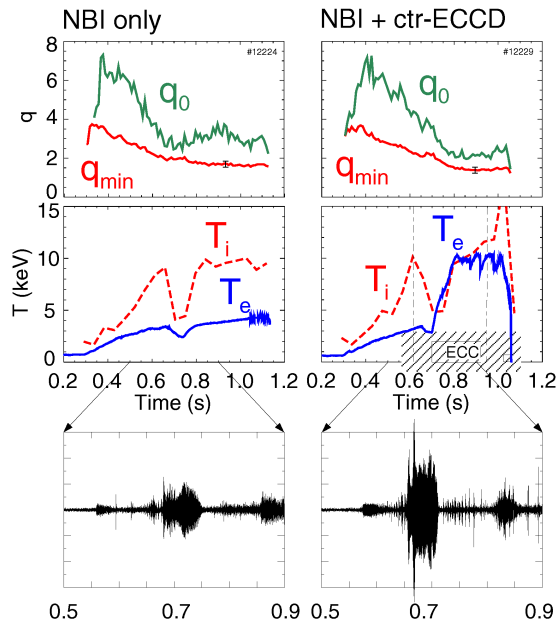


Fig. 10 Comparison of reversed magnetic shear  $L$ -mode discharges with NI heating ( $\rightarrow$ ion ITB) and with NI together with central counter-ECCD ( $\rightarrow$ ion and electron ITB). Time traces of central and minimum  $q$  ( $q_0$ ,  $q_{min}$ ), central temperatures and Mirnov signals for  $n=1$  modes ( $I_p=1$  MA,  $B_t=2.45$  T).

In a fusion reactor, where fast particles predominantly heat the electrons, internal transport barriers must be compatible with  $T_e$  being equal to  $T_i$ . Combining NI and ECRH/ECCD during current ramp up, ITBs of both electrons and ions with  $T_e \approx T_i \approx 10$  keV have been achieved (Fig. 10) [29,32]. By applying central counter-ECCD in an ion ITB discharge also an electron ITB occurs, seen as a strong rise of the electron temperature in Fig. 10, nearly without any change in the peaked profiles of ion temperature, density and toroidal rotation velocity. Despite the fivefold increase of the heat flux into the electrons in the plasma center, neither the electron nor the ion thermal conductivities increase [25,29]. The ITG growth rates obtained from the GLF23 model [17] for the two discharges are again below the poloidal shearing rates. Thereby the destabilising effect for the ITG from the raising ratio of electron to ion temperature is largely compensated by the stabilising Shafranov shift which is larger in the case with ECRH because of the higher electron pressure in the centre.

## 5. Fully non-inductively driven discharge scenarios

Stationary tokamak operation requires the maintenance of the plasma current via a high fraction of internal diffusion driven bootstrap current supplemented by external non-inductively driven currents. We have started to investigate CD scenarios with on-axis CD using nearly perpendicular NI and ECCD at a level of  $I_p=400$  kA ( $q_{95}=9$ ).

### 5.1 High $\beta_p > 3$ discharges with dominant bootstrap CD at Greenwald density

To achieve a high bootstrap current, the poloidal  $\beta$  is maximised by operating at low  $I_p$  [33] and high NI power of 10 MW. Fully non-inductively driven H-mode discharges at high  $\beta_p > 3$  and densities at  $n_{GW}$  have been achieved (Fig. 11). The current in the ohmic transformer is kept constant after reaching the maximum NI power of 10 MW. Here obviously an ion ITB at  $\rho \approx 0.25$  is triggered by the redistribution of fast particles due to fishbones (see Sect. 7.2) [9].

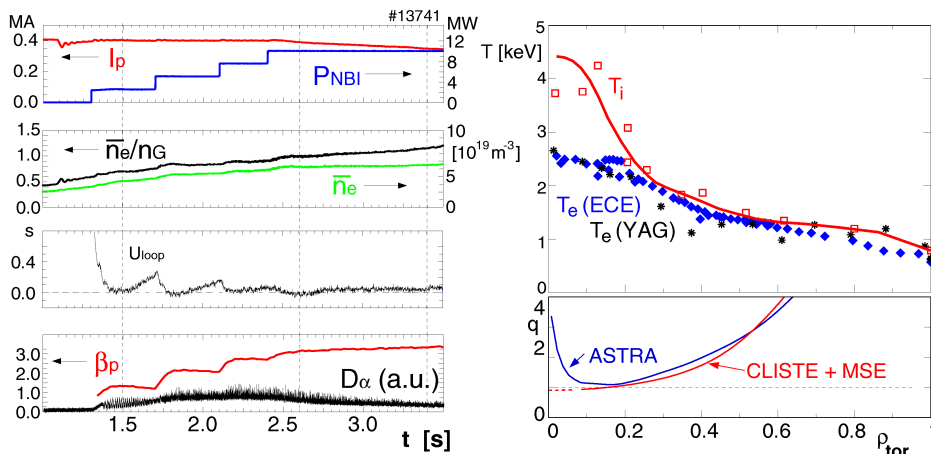


Fig. 11 Time evolution of a fully non-inductively driven H-mode discharge with integrated high performance with respect to  $\beta$ ,  $\bar{n}_e/n_{GW}$  and H factors.  $T$  and  $q$  profiles after 2.6 s show an ion ITB.

This is confirmed by the reduction of the core ion heat diffusivity which is lowest in the high power phase despite the fourfold increase of the heating power. The minimum value at the position of the ITB is  $\approx 0.5 \text{ m}^2/\text{s}$  and is well below the neo-classical values with and without finite orbit width corrections.

The appearance of this ITB coincides with the extinction of the sawtooth activity and - similar to the improved H-mode (1,1) fishbones remain in the plasma, indicating that a  $q \approx 1$  surface is still present. This agrees with the current or  $q$  profiles, inferred from MSE measurements utilising the equilibrium code CLISTE, showing a broad minimum of  $q \approx 1$  in the centre. It agrees reasonably well also with current diffusion simulations using ASTRA and assuming neo-classical conductivity (Fig. 11). Thereby the large bootstrap current fraction reaches  $f_{BS} = 0.56 \pm 10\%$  (error estimated from 10% error in  $T_e$  and  $1.5 < Z_{eff} < 3$ ) and tends to cause negative central shear in the initially monotonic  $q$ -profile. The neutral beam current drives the rest of the plasma current. The plasma current is slightly decreasing due to somewhat decreasing  $\beta_N$  and central MHD activity.

## 5.2 ECCD driven discharges and electron ITB ( $T_e < 15 \text{ keV}$ ) with reversed shear

ECCD has been applied in L-mode plasmas with low current and density optimising the current drive efficiency [9]. ECR waves of three gyrotrons (1.2MW) were centrally launched in either co- or counter-current direction, while the remaining 0.4MW have been used for heating. With the onset of ECRH  $T_e$  rises sharply in both cases, the temperature profiles, however, are distinctly different. While for co-ECCD the temperature gradient in the plasma core is nearly constant ( $T_e(0) \approx 10 \text{ keV}$ ), an electron ITB develops in the counter-ECCD discharge in the presence of a reversed magnetic shear inside  $\rho_t \approx 0.25$ . The electron temperatures go up to 15 keV in the negative shear region (ions remain cold below 1 keV). For electron ITBs reversed shear seems to be a prerequisite [29,34] in agreement with theory of ETG driven turbulence and its possible stabilisation [19]. Continuously irregular (2, 1) modes with a high growth rate cause  $T_e$  collapses and are located near the maximum of the temperature gradient, suggesting a pressure driven ideal mode. As two  $q=2$  surfaces are present in the plasma the mode may be of the double ideal kink structure.

The deposition, propagation and absorption of the electron cyclotron waves has been calculated with the TORBEAM code predicting in both cases a CD fraction of about 80%. This is confirmed by current diffusion simulations predicting for the co-ECCD case an driven  $f_{ECCD} = 0.82$  or 320 kA, respectively, and a nearly fully non-inductive drive ( $f_{BS} = 0.12$ ) [35]. For the counter-ECCD case the strong MHD modes and huge current density gradients did not permit a quantitative assessment.

## 6. Stabilisation of neo-classical tearing modes by ECCD

NTMs are the main  $\beta$ -limiting MHD events in conventional H-mode scenarios with positive shear in ASDEX Upgrade. Their onset  $\beta_N$  scales proportional to normalised gyroradius  $\rho^*$  without significant dependence on collisionality  $\nu^*$  for more than an order of magnitude variation in  $\nu^*$  [3,11,36]. This onset behaviour is consistent with the stabilising terms of the polarisation current model and, if the heat flux limit for parallel heat flow in the islands is taken into account, may also be described with the  $\chi_{\perp}/\chi_{\parallel}$ -model in the generalised Rutherford equation.

In ASDEX Upgrade, NTMs may occur in a sequence of modes. Usually, the final mode is a (3,2) or, at lower densities, a (2,1) NTM [11,12]. An important observation has been that NTMs of different helicities never coexist in a stationary state, which has been modelled using a non-linear cylindrical tearing mode code [11,12].

Stabilisation of NTMs by using ECRH or ECCD is of great importance for next-step experiments, which suffer already at lower  $\beta_N$ 's from NTMs because of the onset scaling given above. On ASDEX Upgrade the amount of ECRF driven current was varied by changing the injection angle, while feed-forward scans in  $B_t$  of 5-10% are used to fine-tune the radial position of the absorption location [37,39]. With about 10% of the total heating power, corresponding to 15 - 20 kA of helical current driven within the island, a (3,2) NTM at  $\beta_N = 2.5$  can be completely stabilised by co-ECCD (Fig.12). The experimental results are in agreement with with a 2 dimensional non-linear cylindrical tearing mode code [49]. The main stabilising effect being the local helical current generated by ECCD. There is no significant difference

between AC and DC stabilisation, while pure ECRH is much less effective in stabilising the mode. In the experiments conducted so far,  $\beta$  does not recover its full value at mode onset, although the mode is completely stabilised. This is attributed to a confinement degradation during ECRH/ECCD in this scenario.

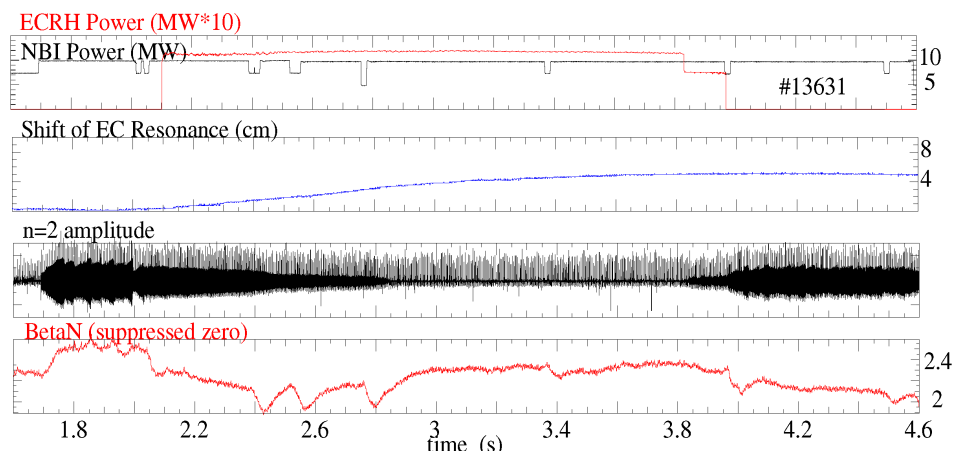


Fig. 12 Complete (3,2) NTM stabilisation with ECCD. Switching off ECCD in steps leads to reappearance of the (3,2) mode and  $\beta$  reduction.

## 7. MHD in advanced Scenarios

MHD instabilities in advanced scenarios limit the accessible operating regime, in particular the maximum  $\beta$  by either terminating the improved confinement or even causing disruptions. Besides this unfavourable role of MHD instabilities, they have been shown to be helpful in both triggering improved confinement and supporting quasi-stationary discharge conditions.

### 7.1 Clamping of $q$ profile and triggering of ITBs

In the absence of sawteeth quasi-stationary discharge conditions are provided by reconnecting (1,1) fishbones in improved H-mode discharges, limiting the peaking of impurity density, electron temperature and also current profile [27,28]. Fishbone oscillations occur at nearly constant frequency, and the eigenfunction  $T/\sqrt{V}$  as derived from electron cyclotron emission show a clear island structure with a phase jump, located at about  $\rho_t=0.2$  for the fishbone considered [10]. In reversed shear discharges with  $q_{\min}>1.5$  fishbones with higher mode numbers ( $m,n > 1$ ) have been observed, in agreement with theoretical predictions. These fishbones have a similar effect on the  $q$  profile. Often (2,1) fishbones clamp the current profile locally, keeping the minimum  $q$  value in the vicinity of 2 for about 100 ms. As for the fishbones in the improved H-mode discharges with flat shear, no degradation in confinement occurs [25].

While after the ITB formation suppression of turbulence can be explained by the sheared poloidal rotation, the dynamics of the ITB formation is not yet well understood. An influence of MHD phenomena in this process appears probable, as the existence of low order rational surfaces has been found to support the ITB formation in various tokamaks [41]. On ASDEX Upgrade a strong influence of fishbone activity on the formation of ITBs has been discovered [10]. In nearly all discharges with a clear ITB its onset occurs right after the first fishbone oscillations, radially located in the vicinity of  $q_{\min}$ . At the same time and radial location the turbulence becomes suppressed, as measured by reflectometry. In discharges without significant MHD phenomena, however, usually no formation of ITBs is observed. The triggering of the ITB is attributed to the redistribution of resonant fast particles caused by interaction between fishbones and fast particles, which results in a current across the corresponding magnetic surfaces. Its return current in the bulk plasma locally drives poloidal plasma rotation, equivalent to a radial electric field, which may lead to the suppression of gradient length limiting micro instabilities. The calculated shearing rate  $\omega_{E \times B}$  indeed exceeds maximum linear growth rate of ITG modes.

That fishbones indeed can suppress turbulent transport is demonstrated in Fig. 13. After a period without MHD activity, a sudden increase in the normalised  $\beta_N$  value occurs right after the onset of  $n=3, m=5\dots 7$  fishbones at about 1.21 s. This ITB evolution is stopped by the

reduction of beam power. The enhancement in  $\beta_N$  is caused by an increased temperature gradient at about  $\rho_r=0.6$ , which coincides with the radial location of the corresponding rational surfaces of the fishbone oscillations at  $\rho_r(q=5/3\dots7/3)=0.53\dots0.68$ .

## 7.2 Limitation of operational regime

In ASDEX Upgrade reversed shear discharges often continuous (2,1) double tearing mode (DTM) activity appears when the minimum q-value reaches 2. These modes lead to the break down of the ITB as seen by decreased temperatures in Fig. 10a between 0.68 and 0.78 s. During the mode activity, the current profile is clamped. The end of the (2,1) activity coincides with a sudden drop of  $q_{\min}$  well below two due to decoupling of the two rational surfaces with the increasing distance between the resonant surfaces. In discharges with combined NI and ECRH the DTM does not appear if the electron heating is provided before the expected onset of the DTM, or disappears as soon as the ECRH is switched on (Fig. 10b).

The sawtooth like events observed on  $T_e$  in Fig. 10b after 0.8 s limit peaking of the temperature profile and are attributed to ideal (2,1) mode activity (growth time about 200  $\mu$ s). This mode was shown to be an infernal mode, driven by the large pressure gradient in the weak magnetic shear region [42]. Coupling of this mode to an external kink mode is responsible for the disruptive termination at 1.1 s. Ideal modes often appear in reversed shear discharges when a low order rational q-value at the plasma edge allows the coupling of the (2,1) infernal mode to an external kink mode. The resulting mode mostly causes a disruption about 1 ms after its onset due to the global character of the eigenfunction as measured by ECE showing a large amplitude at the plasma edge. This eigenfunctions agree very well with those derived from the stability analysis of low m ideal modes.

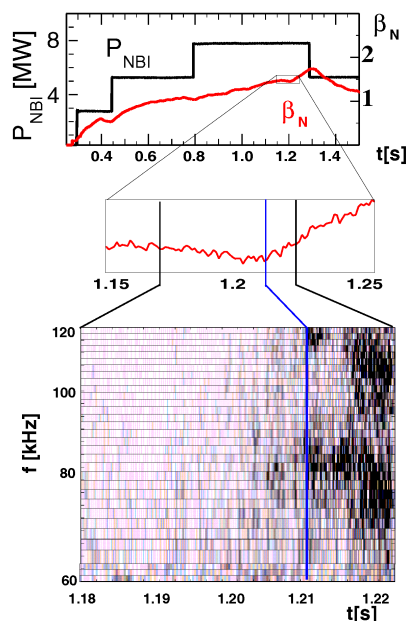


Fig. 13 Wave forms of NI heating power,  $\beta_N$  and wavelet plot of Mirnov signal showing the onset of fishbone oscillations coinciding with the sudden increase in  $\beta_N$ .

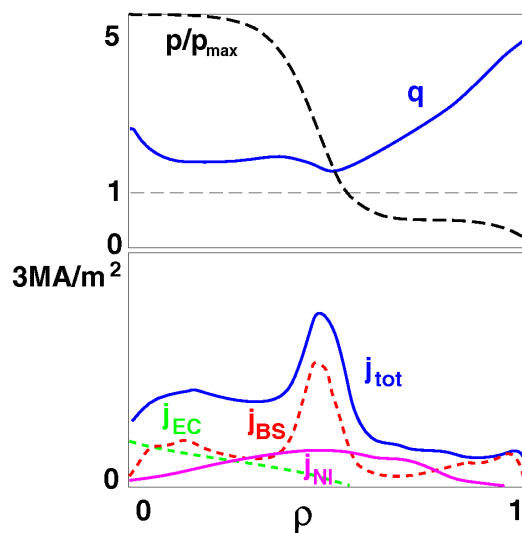


Fig. 14 Pressure, current density composition and q profiles expected for the more tangential NI (5 MW) combined with on-axis ECCD  
Current composition:  $f_{BS}=0.65$ ,  $f_{NI}=0.25$ ,  $f_{EC}=0.10$ .

## 7.3 Extension of the operational regime by non-inductive CD and wall stabilisation

An optimised q-profile with respect to the stability of core localised modes, needs  $q_{\min}>1.5$  (NTMs), distant double rational surfaces (DTMs) and high shear at the low order rational surfaces, especially in regions with large pressure gradients (ideal modes). Furthermore, pressure gradient at the  $q=2$  surface should be kept as low as possible.

Stationary sustainment and control of such magnetic shear scenarios require externally driven currents. Significant modification of the plasma current profile on ASDEX Upgrade was limited so far to early heating in current ramp up or in low density discharges by electron cyclotron current drive with up to 320 kA. The rotation of one of the NI injectors into a more tangential direction carried on right now, will offer the possibility of off-axis co-NI current

drive up to 250 kA peaked around  $p \approx 0.5$  with a rather broad profile (Fig. 14) [25]. To estimate the expected current profiles, besides the external current drive, also the bootstrap current determined by the pressure gradient and depending therefore on the energy transport was taken into account. Assuming either a ITB pressure profile or a reduced transport equal to the neo-classical ion diffusivity inside the  $q_{\min}$ -radius results in pressure profiles as shown in Fig. 14 (including an H-mode edge). The  $q$ -profile shows a broad minimum at  $q_{\min} \approx 1.5$ , avoiding close double low order rational surfaces and having a high shear at  $q=2$ . The plasma current is fully non-inductively driven ( $f_{BS}=0.65$ ,  $f_{NI}=0.25$ ,  $f_{EC}=0.10$ ). But the high pressure gradient destabilizes core ideal modes already at  $\beta_N=1.7$ . Reducing the pressure gradient by a factor of two improves MHD stability of internal modes and beta significantly rises for the current profiles expected with the new injector geometry ( $\beta_N \approx 3$  for a bootstrap current fraction of 35% [10]). But then inductive current drive is needed.

The ultimate limit to the pressure would be given by the onset of  $n=1,2$  and 3 external kink modes, as  $I_i$  is rather small for reversed shear  $q$ -profiles (GATO code). External modes, however, could be stabilised by a conducting wall, in combination with a feedback system, which would have to react on the resistive wall time. On ASDEX Upgrade, at present, the wall is too far away from the plasma edge to provide a significant stabilising contribution. Installing additional wall structures inside the vacuum vessel on ASDEX Upgrade is therefore under discussion right now. Since such a wall would have a 3-dimensional structure allowing for heating and diagnostic access, the resulting influence on MHD stability has to be investigated using 3D stability codes. As a first approximation a continuous wall was assumed at the LFS of the torus. Placing a wall at a distance of 1.4 times the distance of the plasma edge from the plasma centre the external kink stability limit was found at  $\beta_N \approx 3.5$  with the weaker pressure gradient.

## 8) Operation with high-Z wall coatings

Today most experiments are using graphite as plasma phasing components. But high erosion yield and especially co-deposition with tritium put question mark on use of graphite in a fusion reactor. An alternative may be high-Z materials having a high threshold for sputtering and especially tungsten (W) exhibits excellent thermo-mechanical properties and low hydrogen inventories. However central concentrations have to be low because of the high radiation power of high-Z materials. Based on the good experience using tungsten as divertor material in ASDEX Upgrade demonstrating reactor-compatible W-concentrations below  $2 \cdot 10^{-5}$  [44], we follow a step by step strategy for testing tungsten as a first wall material too.

To reduce carbon sputtering (main source is at HFS heat shield) a first step was done by applying siliconisation instead of boronisation for wall conditioning, which resulted in reduced oxygen concentrations as with boronisation and low Si concentration of 0.002 ( $\Delta Z_{\text{eff}} < 0.2$ ) [45]. A second step was done by tungsten coating of  $1.2 \text{ m}^2$  of the HFS heat shield ( $\approx 10\%$  of total area) in the bottom part. Spectroscopically measured central tungsten densities have been always below the detection limit of approx.  $5 \cdot 10^{-6}$  [2]. These concentrations are below the threshold tolerable in ITER and more than a factor of ten below concentrations which might influence the plasma operation of ASDEX Upgrade. The next step will be a mostly tungsten covered HFS heat shield (about  $7 \text{ m}^2$ ) in the next experimental campaign.

## 9. Summary and outlook

In the H-mode both ion and electron temperature profiles are self-similar in agreement with critical ITG transport models combined with TEM physics. Stiff temperature profiles are seen at all densities and for quite different radial power deposition profiles. This implies that plasma stored energy and global confinement are directly coupled with H-mode pedestal pressure, and transport coefficients are constrained by global effects and cannot be determined by local conditions. Density profiles are not stiff, providing reduced confinement at high densities close to Greenwald density, but also confinement improvement with more peaked profiles (improved H-mode). ECRH experiments strongly support the hypothesis that ETG physics with streamers play a strong role in electron transport and result in stiff electron temperatures at low densities and  $T_e \gg T_i$ .

More triangular plasma shapes ( $\delta$  up to 0.4) showed remarkably improved H-mode confinement as the pedestal pressure increases with triangularity due to enhanced MHD stability. Moreover, this high confinement level persists up to  $n_{GW}$  with confinement times close to ITER H98-P scaling. H-mode discharges could be sustained up to very high densities, being 10% above  $n_{GW}$  without HFS pellet injection. These beneficial effects allow the anticipated operational regime of ITER-FEAT close to  $n_{GW}$ . At highest triangularities ( $\delta > 0.4$ ) and close to  $n_{GW}$  a regime with small, high frequency type II ELMs was found, which exhibit full H-mode confinement and promise low power load on divertor in future devices. Closeness to double null configuration and q-operation above  $q_{95} = 4.2$  are required.

Favoured density peaking despite high average densities at  $n_{GW}$  was obtained by controlled gas puffing in NI heated H-mode discharges on a time scale of a second. The needed inward pinch is quite low and may be provided by the Ware pinch. Operational window is limited however at higher core heating as the resulting increasing core energy transport and the particle outward transport are closely linked. A second promising refuelling method is provided by HFS pellet injection, where the existence of localised high- $\beta$  plasmoids and their toroidal drift towards plasma core have been proved. First evidence was gained that pellet launch velocities above 500 m/s lead to particle deposition beyond the ELMing edge region and, therefore, reduced pellet particle and plasma energy loss rates.

In the advanced scenarios emphasis was placed on physics and performance enhancement using extended plasma shape and heating capabilities (NI, ECRH, ICRH). Stationary scenarios with improved core confinement in combination with an H-mode edge and with low central shear ( $q_{min} \approx 1$ ) were extended towards higher plasma densities close to  $0.5n_{GW}$  either by edge gas fuelling or by improved core particle confinement with more triangular plasmas. Higher  $\delta$ 's additionally allowed a performance increase up to  $H_{L-89P} \beta_N \approx 7$  still limited by NTMs. The energy confinement of the improved H-mode can largely be unified with that of standard H-mode, as the increase in energy is due to density peaking at still ITG limited T profiles.

Ion and electron ITBs are obtained in reversed magnetic shear discharges ( $q_{min} > 1.5$ ) mainly with L-mode edge. Suppression of fluctuations driving transport is observed by reflectometry in agreement with the paradigm of stabilisation of the TG driven turbulence by sheared ExB velocities ( $\omega_{ExB} > \gamma_{max, TG}$ ). Correspondingly, core heat transport is strongly reduced, and the experimental ion heat diffusivities agree well with neo-classical transport obtained from Monte Carlo simulations, which are reduced compared with those from standard theory. The ion ITB discharges with strong ion heating using NI have been extended up to  $H_{H-98P} = 1.2$  for 1 s (more than 10 confinement times) at  $T_i \approx 15$  keV. Addition of ECRF for central electron heating and counter-CD allowed the achievement of reactor-relevant simultaneous electron and ion core barriers with  $T_e \approx T_i \approx 10$  keV. No performance reduction of the ion channel was observed.

Fully non-inductive current drive was achieved in an integrated advanced H-mode scenario with NI at high beta ( $\beta_p = 3.1$ ,  $\beta_N = 2.8$ ), Greenwald density and high confinement ( $H_{L-89P} \approx 1.8$ ) but still at low plasma currents ( $q_{95} = 9$ ). An ion ITB is formed contributing to the bootstrap current fraction of 0.56, while the NICD accounts for the rest. Central ECRF in mainly CD mode was applied in low current, low density discharges. Current diffusion and ECCD beam tracing calculations predict for stationary co-ECCD discharges a driven current of 320 kA and a nearly fully non-inductive drive. In case of counter-ECCD, the central magnetic shear reverses and triggers an electron ITB with a central  $T_e$  well above 10 keV.

The MHD investigations placed further emphasis on utilisation of ECCD for control of  $\beta$ -limiting NTMs in conventional H-mode scenarios. NTM mode suppression was possible also with unmodulated CD in the islands O-point with powers of  $\approx 10\%$  of the total heating power ( $f_{ECCD} < 2\%$ ). The main stabilising effect is due to the local helical current generated by ECCD. Pure ECRH is much less effective in stabilising the mode. Significant enhancement of  $\beta$  by this method will require feed-back controlled adjustment of the absorption location because the efficiency depends crucially on the exact positioning.

MHD instabilities play a significant role in advanced scenarios on ASDEX Upgrade. Besides their well known unfavourable role in limiting the operating regime (DTMs, pressure driven infernal modes, external kinks and mode coupling leading to disruptions), they contribute to quasi-stationarity of the current density profile (mainly fishbones), and can even act as a trigger for the formation of internal transport barriers. In particular, fishbones have shown to be able to induce the suppression of turbulent transport by redistributing fast resonant particles which causes a radial electric field and hence stabilising poloidal shear flows. Other MHD

instabilities might have a similar effect, which would explain the preferential formation of ITBs in the proximity of low order rational surfaces.

To extend the operating regime, active control of the current profile is necessary. Off-axis CD with 250 kA will be available next year with more tangential NI. Stable core localised modes seem possible by tailoring weakly reversed magnetic shear ( $q_{\min} > 1.5$ ) allowing for  $\beta_N > 3$ . But  $\beta_N$  limit will then be given by external kink modes, as  $I_i$  is rather small for RS q-profiles. These modes require conducting structures close to the plasma – presently not present on ASDEX Upgrade- in combination with a feedback system to react on the resistive wall time.

Finally, first results from experiments with partly tungsten coated HFS heat shield demonstrated the suitability of tungsten as a material not only at the divertor but also in the main chamber of a fusion device. Main advantages compared with graphite are reduced sputtering and low tritium retention. The next step in ASDEX Upgrade will be a mainly tungsten covered HFS heat shield. This comes together with a divertor adapted to optimal performance at higher  $\delta$ 's.

## References

- [1] Coster D. et al., this conference EXP4/20, submitted to Nucl. Fus.
- [2] Rohde V. et al., this conference EXP4/24, submitted to Nucl. Fus.
- [3] Gruber O. et al., Nucl. Fus. **39** (1999) 1321
- [4] Rytter F. et al., this conference EX2/2, submitted to Nucl. Fus.
- [5] Peeters A. et al., this conference EXP5/06, submitted to Nucl. Fus.
- [6] Lorenz A. et al., this conference PDP/05, submitted to Nucl. Fus.
- [7] Neu R. et al., this conference EXP5/30, submitted to Nucl. Fus.
- [8] Dux R. et al., this conference EXP5/32, submitted to Nucl. Fus.
- [9] Wolf R. et al., this conference EX4/4, submitted to Nucl. Fus.
- [10] Guenter S. et al., this conference EX7/3, submitted to Nucl. Fus.
- [11] Zohm H. et al., this conference EXP4/20, submitted to Nucl. Fus.
- [12] Yu Q. et al., this conference PD/3, submitted to Nucl. Fus. [11]
- [13] Suttrop W. et al., Plasma Phys. Contr. Fus. **39** (1997) 2051
- [14] Stober J. et al., Plasma Phys. Contr. Fus. **42** (2000) A211
- [15] Kotschenreuther M. et al., Phys. Plasmas **2** (1995) 2381
- [16] Tardini G. et al., Proceedings 27th EPS conf., Budapest (2000)
- [17] Waltz R.E. et al., Phys. Plasmas **4** (1997) 2482
- [18] Nordman H., et al., Nucl. Fus. **30** (1990) 983
- [19] Jenko F. et al., Phys. Plasmas **7** (2000) 1904
- [20] Lang P.T. et al., Nucl. Fusion **40** (2000) 245
- [21] Mueller H.W. et al., Phys. Rev. Lett. **83** (1999) 2199
- [22] Lorenz A. et al., Rev. Scient. Instr., in press (Oct 2000)
- [23] Ozeki H., et al., Nucl. Fus. **30** (1990) 983
- [24] Levinton F.M. et al., Phys. Rev. Lett. **75** (1995) 4417
- [25] Gruber O. et al., Nucl. Fusion **40** (2000) 1145
- [26] Gruber O. et al., Phys. Rev. Lett. **83** (1999) 1787
- [27] Wolf R. et al., Plasma Phys. Contr. Fusion **41** (1999) B93
- [28] Guenter S. et al., Nucl. Fusion **39** (1999) 1321
- [29] Wolf R. et al., Phys. Plasmas **7** (2000) 1839
- [30] Lin Z. et al., Phys. Plasmas **4** (1997) 1404
- [31] Shaing K.C. et al., Phys. Plasmas **4** (1997) 771
- [32] Guenter S. et al., Phys. Rev. Lett. **84** (2000) 3097
- [33] Oikawa T. et al., Nucl. Fus. **40** (2000) 1145
- [34] Buratti P. et al., Phys. Rev. Lett. **82** (1999) 560
- [35] Sauter O. et al., Phys. Rev. Lett. **84** (2000) 3322
- [36] Guenter S. et al., Nucl. Fus. **38** (1998) 1431
- [37] Zohm H. et al., Nucl. Fus. **39** (1999) 577
- [38] Gantenbein G. et al., Phys. Rev. Lett. **85** (2000) 1242
- [39] Yu Q. et al., Phys. Plasmas **7** (2000) 312
- [41] Cardoso L. et al., Plasma Phys. Control. Fusion **39** (1997) 303
- [42] Guenter S. et al., Nucl. Fus. **40** (2000) 1541
- [44] Neu R. et al., Plasma Phys. Contr. Fus. **38** (1996) A165
- [45] Rohde V. et al., Europhysics Conference Abstracts (Proc. 26th EPS Conf. Contr. Fus. Plasma Phys., Maastricht (1999), edited by B.Schweer et al., **23 J**, P4.038